Two-Tier Vector-Network-Analyzer Calibrations for Uncertainties in Laboratory-Based Over-the-Air and Channel Measurements

Paritosh Manurkar, *Senior Member, IEEE,* Sudantha Perera, *Member, IEEE,* Kate A. Remley, *Life Fellow, IEEE,* Dylan F. Williams, *Life Fellow, IEEE,* Mohamed Kashef, *Member, IEEE,* Joshua M. Kast, *Member, IEEE and* Robert D. Horansky, *Member, IEEE*

***Abstract*—We present a straightforward and systematic approach for identifying the dominant uncertainties related to vector-network-analyzer measurements of chambers utilized for free-field test of wireless devices. We assess the uncertainty related to long cable runs and discuss the trade-offs between the ease of calibration due to the choice of calibration location and the resulting measurement uncertainty. We illustrate these concepts by assessing the combined uncertainty in the power delay profile and angle of arrival of reflected signals within a hybrid anechoic/reflective chamber for three common calibration locations. The framework presented here allows users to quantitatively consider the trade-offs between uncertainty and ease-of-measurement that are uniquely important to over-the-air chamber-based measurements.**

***Index Terms*—Channel measurement, measurement uncertainty, over-the-air test, vector network analyzer, wireless system.**

I. Introduction

LABORATORY-BASED over-the-air (OTA) and channel test configurations in enclosed chambers are vital to the wireless ecosystem. OTA tests performed in these chambers are used in a number of ways. In order to measure—and calibrate—the transfer function of such chambers, a vector network analyzer (VNA) is often utilized. We introduce a systematic, two-tier approach for evaluating individual components of uncertainty related to VNA calibrations, specifically geared toward OTA and channel test-chamber measurement applications. We illustrate the propagation of uncertainty through to relevant chamber characteristics such as the power delay profile and angle of arrival of reflected signals. The method may be utilized to assess the uncertainty in VNA measurements for the applications that follow and many others.

For applications intended to determine the viability of new wireless devices or subsystems in the design phase or for certification performance assessment, the test chamber is typically precharacterized. This ensures that it meets required specifications such as minimal reflections in the quiet zone of an anechoic chamber or compact antenna test range [1]–[5] or spatial uniformity in the working volume of a reverberation chamber or hybrid anechoic/reflective chamber [6]–[10]. Once characterized, the chamber's transfer function is then corrected out from the measurement in post processing in order to assess the device or system under test. We refer to these as "OTA measurements" below.

Other applications utilize the test-chamber's response as the primary output. These include channel-emulation approaches that create the temporal and/or spatial characteristics of specific propagation-channel conditions within the laboratory environment. A sampling of these applications includes emulation of reflective channels or test artifacts for industrial and other wireless applications [11]–[13], specific field or plane-wave-spectrum generation [14], [15] and verification of channel sounders or other instruments by use of a reference measurement [16], [17]. These applications are finding increased use for testing mmWave devices with active and beamforming antennas [18] and are referred to as "channel measurements" below.

Two aspects of VNA calibration and measurement are uniquely important in OTA and channel testing. First is the choice of the physical location of the end of the cable where the calibration standards are connected, here termed the "calibration location." Due to cable flexibility, the calibration location may be different from the location where the chamber transfer function, channel or DUT is measured, which we call the "measurement location." We refer to the "calibration reference plane" as the electrical plane in a coaxial connector or rectangular-waveguide flange at which the VNA is calibrated. If the coaxial connector or rectangular-waveguide flange is connected to a flexible cable and is moved, the calibration reference plane moves with the connector or flange. A second key aspect for OTA and channel testing is antenna-fixture and/or cable movement, either during the calibration or during the measurement itself. Besides these two aspects, other uncertainty components such as connector repeatability, drift, linearity, and noise also present different challenges compared to a typical VNA calibration.

In test chamber measurements, trade-offs may need to be considered in the choice of the calibration location. These include user access to antenna fixtures within the chamber, a specific application's requirements on overall measurement

Paritosh Manurkar is with the Department of Physics, University of Colorado, Boulder, CO 80309, USA and is an Associate at the National Institute of Standards and Technology, Boulder, CO 80305, USA (e-mail: paritosh.manurkar@nist.gov).

Kate A. Remley, Dylan F. Williams, Joshua M. Kast and Robert D. Horansky are with the National Institute of Standards and Technology, Boulder, CO 80305, USA (e-mail: kate.remley, dylan.williams, and robert.horansky@nist.gov).

Sudantha Perera is with Advanced Radar Research Center (ARRC), University of Oklahoma, Norman, OK 73019, USA

Mohamed Kashef is with the National Institute of Standards and Technology, Gaithersburg, MD 20899 USA (e-mail: mohamed.kashef@nist.gov)

Manuscript received August 13, 2025; revised September 17, 2025,accepted September 22, 2025.

U.S. government work not protected by U.S. copyright.

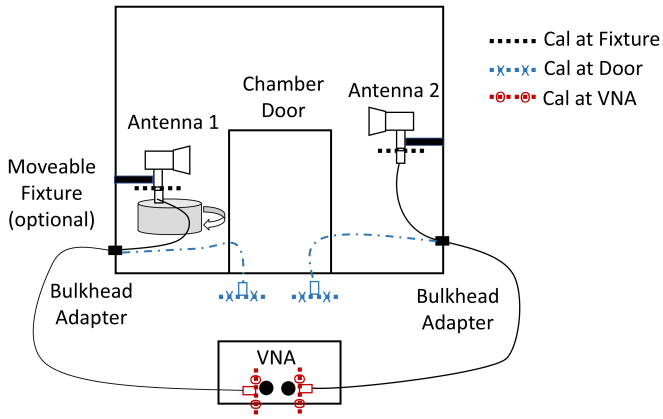

Fig. 1. Three common calibration approaches for OTA test chamber characterization. A VNA located outside the chamber is connected to antennas by coaxial cables passing through bulkheads in the chamber. Locations corresponding to the three calibration approaches discussed in the present work are indicated by the three line types. In the example shown here, Antenna 1 is placed a rotating table, which will introduce cable movement during a measurement. The uncertainty due to cable movement can be precharacterized by use of the method described in the present work.

uncertainty, and whether the application requires movement of cables and/or antenna fixtures during measurement.

As an example, three common calibration locations are illustrated in Fig. 1. Calibration standards may be connected to the connectors at the ends of the coaxial cables that attach to the antenna fixtures ("Cal at Fixture," black dashed line), or the cables may be brought to the door of the chamber for convenience ("Cal at Door," blue dashed line with X's) at the expense of additional cable movement. Finally, if the setup configuration doesn't change from measurement to measurement, the calibration may be carried out at the VNA ports ("Cal at VNA," red dashed line with circles). For this last configuration, the cables and adapters between the calibration location at the ports of the VNA and the antenna fixture are measured and then de-embedded in post processing. For fixed setups, this choice of calibration location is very convenient, but at the expense of additional uncertainty related to the measurement of the coaxial cables and adapters.

Cable bending is also important because OTA and channel chamber setups often include long coaxial cable runs leading from outside the chamber to antennas mounted on fixtures inside the chamber. As a result, the uncertainty in the calibration of the VNA is often dominated by errors due to cable bending. The "Cal at Door" location in Fig. 1 is an example of this, where the calibration is performed with the coaxial cables near the door, a significantly different location than that of the cable during measurement. As well, when the application requires antenna movement, additional uncertainties may need to be identified (for example, when the measurement uses a synthetic-aperture array [19] or a turntable where the antenna moves to different locations during the measurement sequence).

The two-tier VNA calibration approach presented in this paper provides a methodology to identify and precharacterize these and other components of uncertainty, allowing users to select the calibration location that best meets their needs. We consider repeatability and reproducibility for calibrations performed in configurations with long cable runs, the effect of cable movement, and the corresponding impact on measurement uncertainty in typical OTA and channel test applications. While prior work discusses uncertainties in VNA calibrations for OTA and channel measurements [9], [16], [17], [19], [20], the two-tier approach lends itself to precharacterization of components of uncertainty for many such applications and remains, to the best of our knowledge, unpublished.

In Section II, we introduce one- and two-tier VNA calibration approaches and apply them to typical OTA and channel chamber configurations. In Section III, we present methods for identifying and precharacterizing specific components of uncertainty related to these configurations. Section IV illustrates the combined uncertainty for each of the calibration locations shown in1. To demonstrate the impact of these choices of calibration location, in Section V we apply the two-tier approach to two common use cases: a power delay profile for a single receive antenna within a hybrid reflective/anechoic test chamber and for determining the angle of arrival for reflections within the chamber as measured with a synthetic-aperture receive array. We show that the choice of calibration location can have a significant impact on the uncertainty in the PDP, primarily due to cable bending. We also illustrate that the choice of calibration location for the synthetic-aperture measurement may have a negligible impact on the angle of arrival because the synthetic aperture is based on relative phase measurements across the aperture.

II. VNA Calibrations for OTA and Channel Measurements

In this section, we introduce a two-tier VNA calibration approach [21]–[23] that allows users to both correct measured S-parameters and propagate the corresponding uncertainties through to the final result. The method starts with a first-tier VNA calibration that maps raw measurements performed by the VNA to corrected data at a measurement reference plane (the location, usually at a connector interface, to which the VNA is calibrated to make corrected measurements). We then perform a second-tier calibration that is perturbed in some way from the first-tier calibration to evaluate additional sources of uncertainty, such as connection repeatability, calibration reproducibility or cable bending during scanning-state measurements.

To simplify the procedures, we use 8-term calibration models based on "wave-parameter" measurements of the forward and backward wave amplitudes at each port of the VNA. This allows for the use of the same four-port scattering-parameter error model in both the first-tier and second-tier calibrations. However, we note that everything described in this article can be accomplished with first-tier VNA calibrations determined from scattering-parameter and switch-term measurements, followed by second-tier scattering-parameter calibrations. In this case, the first-tier-corrected measurements determined by the first-tier calibrations are used to determine corrected scattering parameters that are then further corrected by the second-tier calibrations, as before.

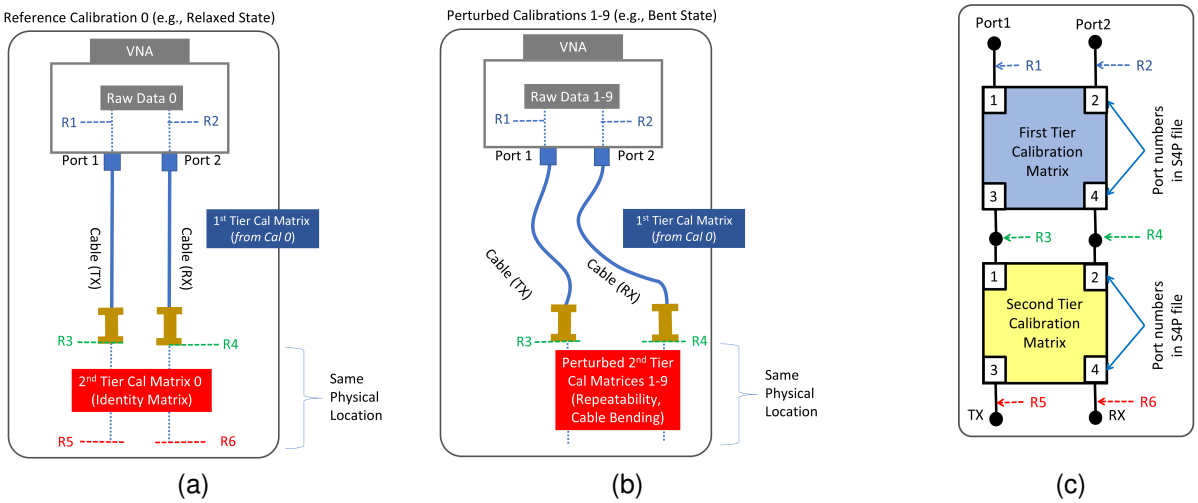

Fig. 2. Illustration of first- and second-tier VNA calibration matrices. (a) The first-tier reference calibration transforms raw data measured at R1 and R2 to reference planes R3 and R4 located at the ends of the coax-to-waveguide adapters. Second-tier calibration matrices are derived from a set of perturbed calibrations 1–9. The perturbations capture effects such as repeatability or, as shown here, cable bending. (c) Graphical representation of the cascaded two-port calibration matrices in (a) and (b). Second-tier calibration matrices represent various non-idealities in the measurement set-up. Note that the cables are shown parallel only for illustration purposes.

The method requires performing several sets of second-tier calibrations in order to determine the variation in the perturbed calibration matrices. During these repetitions, the first-tier calibration may be left unchanged, or it may be repeated each time, depending on the sources of error that are being evaluated. To implement the method, we must clearly define the locations at which the calibrations and the measurements are performed, as discussed below.

A. First- and Second-Tier Calibrations

Fig. 2 shows an example of how we can form the first- and second-tier calibrations. The example shown in Fig. 2 illustrates the characterization of uncertainty due to cable bending for an OTA scenario, but the procedure is similar for finding other components of uncertainty related to, for example, repeatability and reproducibility. First, a reference calibration (here termed "Calibration 0") was carried out. Then several perturbed calibrations ("Calibrations 1–9") were performed at reference planes R3 and R4. Perturbations could include bending the cable over the range expected during measurement, movements reproducing the calibration, or connection repeatability.

The reference calibration (Calibration 0) was used to derive the first-tier calibration matrix that corrected for the non-idealities of the test set-up to the first-tier reference planes R3 and R4. As well, the first-tier calibration was used to correct the raw VNA data labeled "Raw Data 0" in the figure.

The first-tier calibration was performed by measuring calibration standards with known electrical characteristics at measurement reference planes R3 and R4. The first-tier calibration matrix was formed from these measurements. The first-tier calibration matrix may include systematic calibration uncertainties and may include large corrections to correct for non-idealities in the VNA hardware, as well as correcting for the test-port cable amplitude and phase. In the calculation of the calibration matrix, arbitrary root choices are made at each frequency.

Note that the calibration matrices in our technique are typically represented as 4-port (s4p) files that map the two-port raw measured data at, for example, reference planes R1 and R2 to calibrated two-port data at R3 and R4. While these calibrations could be represented by two two-port calibration matrices, we combined these two two-port calibration matrices in post-processing to obtain easily cascadable four-port matrices.

B. Use of Second-Tier Calibration Matrices to Evaluate Uncertainty

In the previous section we measured a collection of .s4p scattering-parameter calibrations comprised of a single reference calibration (Calibration 0 in Fig. 2) and a number of perturbed calibrations (Calibrations 1–9 in Fig. 2). The perturbed calibrations captured the differences in the calibrations due to non-ideal effects such as cable bending, connection repeatability, reproducibility of a calibration. As described in Section III, these setup-related components of uncertainty may often be precharacterized. Because the second-tier calibrations were used to evaluate the uncertainty in the measurement, their deviations from ideal transparent scattering-parameter matrices were, therefore, typically much smaller than the first-tier corrections. Thus, the root choices were generally unambiguous.

In our procedure, collections of these individual second-tier calibration matrices were combined to capture components of the total VNA calibration uncertainty that could ultimately be propagated into the measurements. To do this, we used the "Combine" function [24] of the NIST Microwave Uncertainty Framework [25] to combine the uncertainty from the changes

in the second-tier calibration matrices due to various perturbations, using the "Select result name" pull-down menu item to ensure that the Combine function uses different seeds for each independent error mechanism.

As an example, as illustrated in Fig. 2, to quantify cable bending, we performed nine perturbed second-tier, two-port measurements $[S]_{mech_x,P_y}$ of the calibration standards, where "$mech_x$" represents the xth uncertainty mechanism being assessed. P_0 represents the Reference Calibration 0 that was conducted with the cable measured in a relaxed state as shown in Fig. 2a, and P_y for y=1 ... 9 represents the set of nine perturbed measurements shown in Fig. 2b. The perturbations did not maintain the same bend radius as the relaxed state. They were instead constrained to the expected movements involved in each calibration scenario (e.g., moving a cable from the antenna fixture to the door in a manner that would be used for each calibration), and, thus, nine was deemed an adequate number.

The nine calibration matrices were combined as described in [24] to form the second-tier calibration matrix (or "error box") with the uncertainties associated with a specific error mechanism such as cable bending. Figure 2c illustrates the cascade of the first-tier and second-tier calibrations in graphical form for an OTA or channel measurement. The cascading process is described in more detail in the Appendix, with Fig. 15 illustrating the general cascade of the first- and second-tier calibrations in flow-graph form.

A complete VNA calibration model with a full set of associated uncertainty mechanisms can be assembled by cascading individual four-port calibration networks and their associated uncertainties. We used the NIST Microwave Uncertainty Framework [25] to accomplish the task of cascading individual four-port calibration networks and propagating their associated uncertainties through the cascade process. Finally, we applied these calibrations to correct measured data and accurately propagated these uncertainties to the calibrated measurements in which we were interested.

Note that we can evaluate the statistics of any quantity generated at any point in the process, whether they be the uncertainties of elements of individual or cascaded calibration matrices, or the uncertainties in calibrated scattering parameters. For example, we can calculate the mean and variance of the phase of the transmission terms of the cables due to bending, connection repeatability, or both. We can also evaluate correlations between the various components of uncertainty, if desired. In addition, we can calculate the mean and variance of the phase of the transmission terms of the calibrated scattering parameters of the channels we wish to measure. See the Appendix for details on evaluating the second-tier calibration matrices from a series of two-port calibrations.

III. EVALUATING COMPONENTS OF UNCERTAINTY FOR OTA AND CHANNEL TEST-CHAMBER MEASUREMENTS

Here we describe methods for identifying components of uncertainty related to the use of a VNA in OTA and channel test-chamber measurements utilizing the two-tier approach described in Section II-B. First-tier calibration matrices, which are typically performed for all VNA measurements, initially correct measurement data for the non-idealities of the VNA and system components up to the first-tier reference planes. Many uncertainties due to variations in manufacturing of the calibration standards and VNA drift related to the first-tier calibration are added automatically at this time by the NIST Microwave Uncertainty Framework [25] we used.

After correcting the multiple perturbed calibration-standard measurements with the first-tier calibration matrix, we used second-tier calibrations to capture uncertainties not already included in the first-tier calibrations, such as cable bending. The ensuing calibration matrices are used to evaluate the uncertainties around the unperturbed state. These uncertainties contribute to the combined uncertainty in the final measurement of the chamber transfer function or channel.

As mentioned previously, uncertainty components including connector repeatability, drift, linearity, noise, and cable movement present different challenges in an OTA test environment compared to a VNA calibration. Not only do we capture noise by performing repeated measurements, linearity by setting up the VNA at its normal operating range, drift and repeatability as described in Sections III-A and III-B, reproducibility in Section III-C, cable movement in Section III-D, fixture motion in Section III-E, but we also, quite importantly, propagate these uncertainties while maintaining any correlations in the uncertainty components by using the NIST Microwave Uncertainty Framework. With this knowledge, a user can make an informed choice of the calibration location and its impact on the measurement uncertainty.

A. Drift and Uncertainty in Calibration Standards

The drift and uncertainty in calibration standards are not based on the two-tier framework. The estimate of drift is based on two first-tier calibrations that are performed before and after each set of measurements of the chamber's transfer function or channel. The deviation in the chamber measurements, when corrected by these first-tier calibration matrices, may be used to estimate the uncertainty due to drift. We used a built-in function in the NIST Microwave Uncertainty Framework to derive the VNA drift from these first-tier VNA calibrations. Such drift encompasses both the natural drift of the instrumentation as well as temperature effects that may have occurred over the duration of the measurement. In particular, in a closed chamber and for a long-duration synthetic-aperture channel measurement, the temperature can rise significantly, affecting the electrical performance of the cables, adapters, and other components in the measurement set-up. Thus, drift can be a significant contributor to overall uncertainty in OTA and channel measurements. Although the calibrations performed before and after the measurements may not capture cyclical drift during long measurements in the chamber, they do capture the long-duration temperature changes we observed.

Another potentially significant contributor to the uncertainty in a channel or DUT measurement corresponds to imprecise knowledge of the exact dimensions of mechanical VNA calibration standards. This component of uncertainty, discussed in

more detail in, for example, [26], can be evaluated from Monte Carlo analyses based on knowledge of the manufacturer's nominal tolerances for each mechanical calibration standard. We also used built-in functions of the NIST Microwave Uncertainty Framework to evaluate and include these components of uncertainty in the first-tier calibrations.

We next utilize the two-tier approach of Section II-B to evaluate components of uncertainty that are specific to VNA calibrations related to OTA and/or channel use cases. By use of the two-tier calibration approach, these components of uncertainty may be precharacterized and the resulting error box applied during subsequent measurements made with the same measurement set-up. We first describe specific steps measuring and calculating the two-tier calibration matrices described in Section II-B. We then provide detailed methodology for evaluating the specific components of uncertainty calibration repeatability, calibration reproducibility, cable and adapter de-embedding, and fixture motion. The application of these components of uncertainty to various calibration approaches will be provided in Section IV.

B. Calibration Repeatability and Noise

The connection of calibration standards during the calibration procedure will vary, even if only slightly, from calibration to calibration. Differences can occur due to subtle changes in positioning and applying torque to the connectors, as well as small cable movement during the measurement of the various standards, especially the Thru. We refer to these differences as *calibration repeatability*.

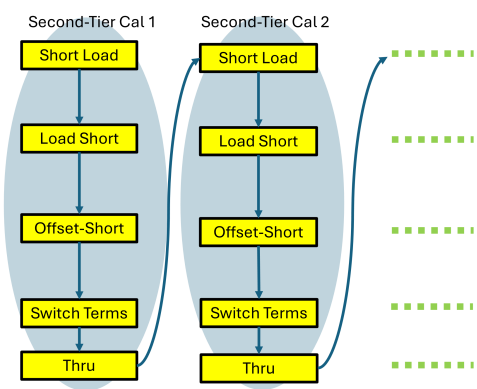

Fig. 3. Second-tier calibration procedure for identifying calibration repeatability. Combinations of calibration standards are connected as for a standard, first-tier calibration. The calibration procedure is repeated several times, each denoted by a blue oval, with green dots signifying continuing sets of perturbations. "Short Load" and "Load Short" refer to calibration standards connected to ports 1 and 2, respectively.

The procedure for obtaining the second-tier calibration matrix related to calibration repeatability is illustrated in Fig. 3. Measurements of the set of calibration standards are repeated several times one after another under test conditions designed to minimize drift and cable bending so as to minimize double counting errors. Repeated measurements also capture the noise. After correcting the measured data by the first-tier calibration matrix, second-tier calibration matrices are formed for each repeat. The deviations between these calibration matrices are used to evaluate the uncertainty due to the perturbations introduced by each repeat.

This component of uncertainty is sometimes quite small when the calibration is performed at the VNA ports or the antenna fixtures. It may be larger for calibrations performed far from the antenna fixtures due to the increased cable movement.

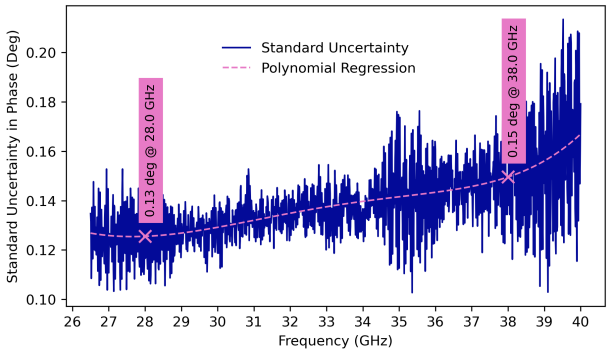

Fig. 4. Standard uncertainty in the phase of $S_{53,P}$ (defined in Fig. 2a) for a calibration repeatability study. The uncertainty was evaluated using the combination of nine second-tier perturbed calibration matrices. The regression is for visualization only and is not used in our analysis.

In the results of a typical calibration repeatability study illustrated in Fig. 4, waveguide standards were connected to a coax-to-waveguide adapter (2.4 mm female to WR-28 waveguide) at the end of a 3.11 m cable. The measurement corresponds to the "Cable (TX)" in Fig. 2. The adapter was attached to a stationary antenna fixture, similar to the black dashed line reference plane in Fig. 1. Nine repeat (perturbed) calibrations were conducted in addition to the first-tier calibration using the method shown graphically in Fig. 3. After correction by the first-tier calibration matrix, the second-tier calibration matrices were computed and combined to evaluate the standard uncertainty.

Between 26 GHz and 40 GHz, the standard uncertainty in magnitude was less than approximately 0.1 dB and the phase was less than approximately 0.2°, with the latter shown in Fig. 4. The cable movement introduced the largest uncertainty. In our configuration, it was particularly large for the thru standard since it required more movement of the cables for the thru measurement at the chamber door.

C. Calibration Reproducibility

As illustrated in Fig. 1, it is sometimes more convenient to perform the calibration for an OTA or channel measurement at a location removed from the antenna fixtures. This may occur, for example, when the choice is made to disconnect the cables from the antenna fixture in order to perform the calibration at the door of a chamber due to a lack of easy access to the antenna fixture, as illustrated by the blue-dashed reference plane in Fig. 1. In this case, the calibration location of the cables near the door will differ from the measurement location when they are reattached to the fixtures. This component of uncertainty is termed calibration reproducibility. Figure 5 illustrates the approach for estimating calibration reproducibility. It should be noted that it was desirable to maintain approximately

the same bend radius when connecting the cable back at the antenna fixture.

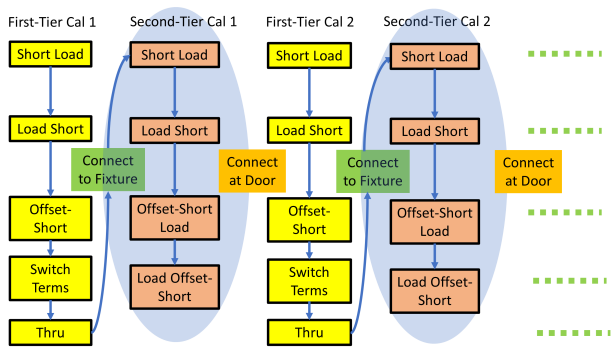

Fig. 5. Procedure for identifying calibration reproducibility. A full first-tier calibration is performed at the door of the test chamber. A partial second-tier calibration is performed at the antenna fixture. The procedure is repeated multiple times, each denoted by a blue oval, with green dots signifying continuing sets of perturbations. "Short Load" and "Load Short" refer to calibration standards connected to ports 1 and 2, respectively.

Because this component of uncertainty is intended to capture the effects of cable bending that occurs between the calibration at the door and the use-case measurement at the fixture, several pairs of first-tier (door) and second-tier (fixture) calibrations are performed, as illustrated in Fig. 5. The second-tier calibration matrix then captures the difference between the initial calibration at the door and measurement location at the fixture. For our calibrations, the Thru and Switch Terms obtained from the first-tier calibration are utilized for the second-tier calibrations. Because these terms simply set the phase of the forward and reverse transmission terms equal, as must be the case due to reciprocity, this is allowed. As was done to assess repeatability, the associated uncertainty is calculated from the differences between the multiple, first-tier-corrected second-tier calibrations performed at the door and the fixture.

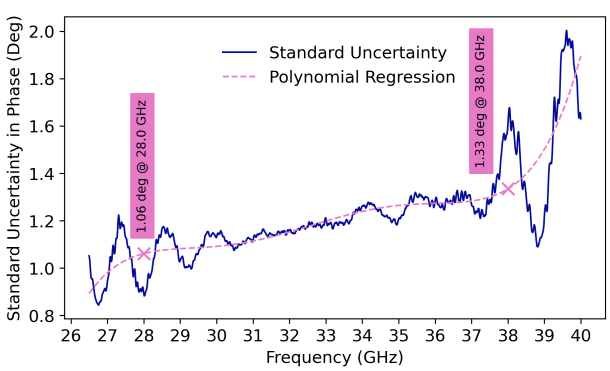

Fig. 6. Standard uncertainty in the phase of $S_{64,P}$ (defined in Fig. 2a) for a calibration reproducibility study. The regression is for visualization only and is not used in our analysis.

Fig. 6 illustrates the results of a calibration reproducibility study utilizing WR-28 waveguide standards that were connected to a 2.4 mm coax-to-waveguide adapter at the end of a 2.1 m cable in our test chamber. The measurement corresponds to the "Cable (RX)" in Fig. 2. The first-tier calibrations were performed at the door of the chamber (R3 and R4 as shown in Fig. 2), and then the coax-to-waveguide adapters were attached to the stationary TX and RX antenna fixtures (R5 and R6). Nine repeat (perturbed) calibrations were conducted at the fixtures, the second-tier calibration matrices were calculated and then combined to evaluate the standard uncertainty.

The results in Fig. 6 show the second-tier phase error at the RX reference plane R6. The phase error is approximately 1.2° at 33 GHz, rising to 1.9° at 40 GHz.

D. Cable and Adapter Measurement and De-embedding

When access to the antenna fixtures or cables inside the chamber is difficult and the chamber configuration does not change from measurement to measurement, it may be most efficient to precharacterize the cables and adapters between the VNA and fixture, which are then de-embedded from subsequent measurements. For a measurement of the chamber or channel, the first-tier calibration would then be performed at the VNA ports outside the chamber.

The cables and coax-to-waveguide adapters are characterized in different sets of measurements. For each, the VNA is first calibrated with a standard first-tier calibration. If the calibration requires different connector types, an "unknown thru" calibration [27] may be used. To assemble the second-tier calibration matrix, we insert the elements S_{11}, S_{21}, S_{12} and S_{22} of the 2×2 scattering-parameters of the cable (or adapter) measured on port 1 into the second-tier calibration matrix at locations $S_{33,P}$, $S_{53,P}$, $S_{35,P}$ and $S_{55,P}$, respectively (see Appendix and top row of Fig. 15). Likewise, we insert the elements S_{11}, S_{21}, S_{12} and S_{22} of the 2×2 scattering-parameters of the cable measured on port 2 into $S_{44,P}$, $S_{64,P}$, $S_{46,P}$ and $S_{66,P}$, respectively (see bottom row of Fig. 15). Again, multiple measurements are performed and inserted into second-tier calibration matrices, with perturbations capturing connection repeatability and the expected cable movement from the door to the fixture and back to the calibration plane or connection repeatability for the adapter.

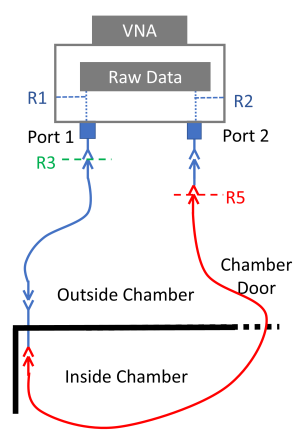

Fig. 7. Approach for characterization of the "Cable (TX)" connected between reference planes R3 and R5. Our set-up consisted of components using both the 2.92 mm connector type (blue) and the 2.4 mm connector type (red). The section of cable inside the chamber was 3.11 m.

Fig. 7 illustrates the measurement set-up for characterization of the TX cable shown in Fig. 2a and 2b. The complete

"TX cable" actually consists of two shorter cables and various adapters that utilize two connector types. In Fig. 7, blue refers to the 2.92 mm connector type and red refers to the 2.4 mm connector type. The entire cable assembly is characterized together. A similar characterization procedure would be carried out for the "RX cable" and the coax-to-waveguide adapters at the antenna fixtures within the chamber.

The standard uncertainty is computed individually for the cables and adapters from the second-tier calibration matrices, as described in Section II-B. The uncertainties associated with the cable and adapter measurements are subsequently cascaded into the combined uncertainty of the channel or DUT measurement. This is discussed in more detail in Section IV-C.

Ultimately, to perform a chamber or channel measurement, a first-tier calibration is performed at the VNA port (R3 in Fig. 7). The S-parameters associated with the cables and adapters are then de-embedded from the measurement in post-processing, transforming the measured S-parameters to the antenna port (R5 in Fig. 7), as desired.

E. Fixture Motion

In some OTA or channel test procedures, the antenna fixture itself moves during a measurement. This can occur, for example, when creating a synthetic aperture [11], [16], [19] (as discussed here) or when the antenna is mounted on a turntable or other movable stage [5], [10], [18]. The uncertainty due to antenna-fixture motion, primarily the effects of cable bending, may be assessed through the second-tier calibration matrix approach, and is then included in the overall uncertainty analysis.

Assessing the uncertainty caused by cable bending due to fixture motion requires that we perform second-tier calibrations at all anticipated antenna-fixture locations, for example, over all locations in a synthetic-aperture scan or all turntable locations. Unlike the uncertainties discussed in Sections III-B,III-C,III-D, a different calibration matrix will be obtained for each antenna-fixture location. In many cases, two sets of calibration matrices are required, one for vertical polarization and one for horizontal polarization of the antenna fixture.

The first-tier calibration is performed at the end of the cable (or coax-to-waveguide adapter) that is connected to the movable antenna fixture. With the antenna removed, calibration standards are connected to the end of the cable or adapter while the fixture is positioned at a convenient reference location such as the center point of the synthetic aperture. It was desirable to keep approximately the same bend radius when connecting the cable back to the antenna fixture. We also found that after connecting it back, the cable required a relaxation time of an hour to reach its previous relaxed state. Then, second-tier calibrations are performed by again connecting the calibration standards to the end of the cable or adapter and stepping through all locations covering the physical range of antenna-fixture states. Using the procedure discussed in Section II-A, the first-tier calibration is used to correct the second-tier measurements of calibration standards at all other antenna-fixture locations. The second-tier calibrations, thus, capture the uncertainty due to cable bending during fixture motion.

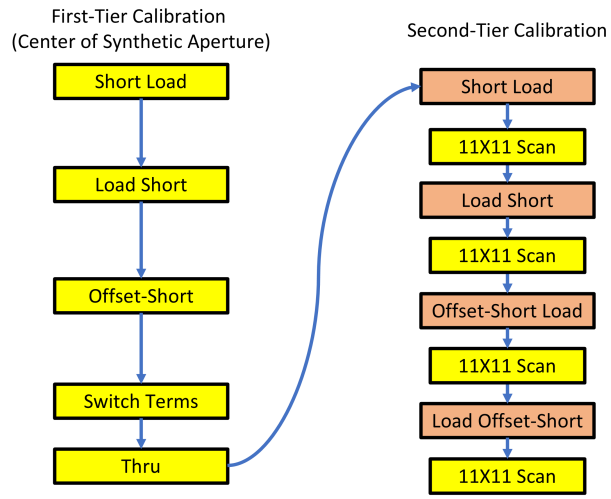

Fig. 8. Procedure for identifying cable-bending uncertainty due to fixture motion. A full first-tier calibration is performed at the center of the planar array. A series of partial second-tier calibrations are then performed while the fixture goes through its range of motion. "Short Load" and "Load Short" refer to calibration standards connected to ports 1 and 2, respectively.

Fig. 8 shows this procedure graphically. For the case illustrated here, the first-tier calibration was performed at the center of a synthetic-aperture array by connecting WR-28 calibration standards to a coax-to-waveguide adapter at the end of a 2.1 m cable ("Cable (RX)" in Fig. 2a). The robotic arm was then moved through an 11×11 synthetic-aperture scan and VNA measurements were made of each standard.

The synthetic aperture discussed here is used to measure propagation-channel effects, as will be illustrated in Section V. It consisted of a 35×35-point planar array created by a robotic arm. This results in 1225 measurement points. To reduce measurement and calculation time for the fixture-motion calibration uncertainty, the coarser 1×11-point array covering the same spatial extent of the larger array was used. We computed 121 (11×11) second-tier calibration matrices, which were then interpolated to the final synthetic-aperture locations. This resulted in 1225 calibration matrices, each applied in post processing.

The cable bending due to fixture motion associated with horizontal and vertical polarizations will be different due to differences in cable bending in the two polarizations. This is shown in the photographs in Fig. 9 for (a) vertical (V) polarization and (b) horizontal (H) polarization of the WR-28 waveguide-to-coax adapter mounted on the robotic-arm antenna fixture. Our analyses have shown that there is a significant cable relaxation time, on the order of one hour, between the H and V measurements. Consequently, as a best practice we perform calibrations and measurements in the H and V polarizations separately. The results for a V polarization measurement are shown here.

To illustrate the procedure for finding uncertainty due to fixture motion, first- and second-tier calibrations were performed on five calibration data sets to yield a nominal average

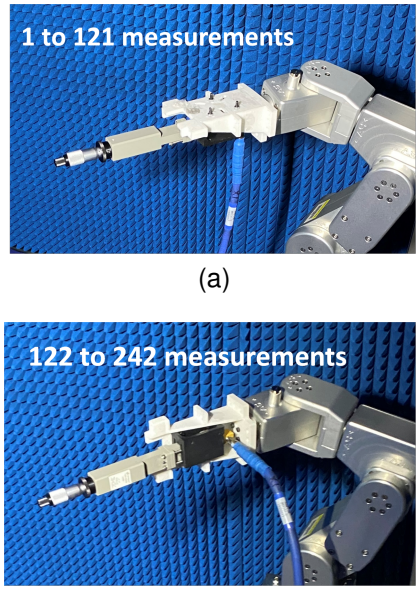

Fig. 9. Robotic arm holding the antenna fixture used in a 28–40 GHz synthetic aperture. (a) vertical and (b) horizontal orientation of the antenna fixture. The coaxial cable connector is not as well-supported in the horizontal polarization (b) as in the vertical polarization shown in (a).

along with the associated uncertainty. These calibrations were performed with a VNA frequency step of 10 MHz, the same that was used in our channel measurements. The distribution of measurements at each synthetic-aperture location were treated as correlated so that when combined in a Monte Carlo uncertainty analysis, the same points from each distribution were used.

The second-tier phase errors are illustrated in Fig. 10 for the V polarization at the four outer locations of the planar array. The 10-hour measurements were performed over a 13-day period. For these measurements, a systematic phase error less than 1° can be seen for different locations in the array, with an even smaller (generally less than 0.5°) phase error due to repeatability of the measurements. We corrected the systematic errors at each location in the array and incorporated the residual repeatability error into the uncertainty calculation.

As shown in Fig. 10, for this particular measurement setup, the phase error due to fixture motion of the robot was quite small. This is, in part, because for our channel-measurement application the robotic arm swept only 127.5 mm on each side with a spatial step size of 3.75 mm, corresponding to $\lambda/2$ at 40 GHz. As well, we developed best-practices that allow for chamber warm-up and cable relaxation time between calibration and measurement. Empirical studies found that the chamber warm-up was on the order of 12 hours and the cable relaxation was on the order of 1 hour. While these best practices enabled a small phase error for our calibrations, for other test-chamber measurement set-ups, the phase error may be larger.

To apply this component of uncertainty to a channel measurement, the spatially coarse, frequency dependent error corrections and associated uncertainties were spatially interpolated to give corrections for the 35×35 grid. The interpolation

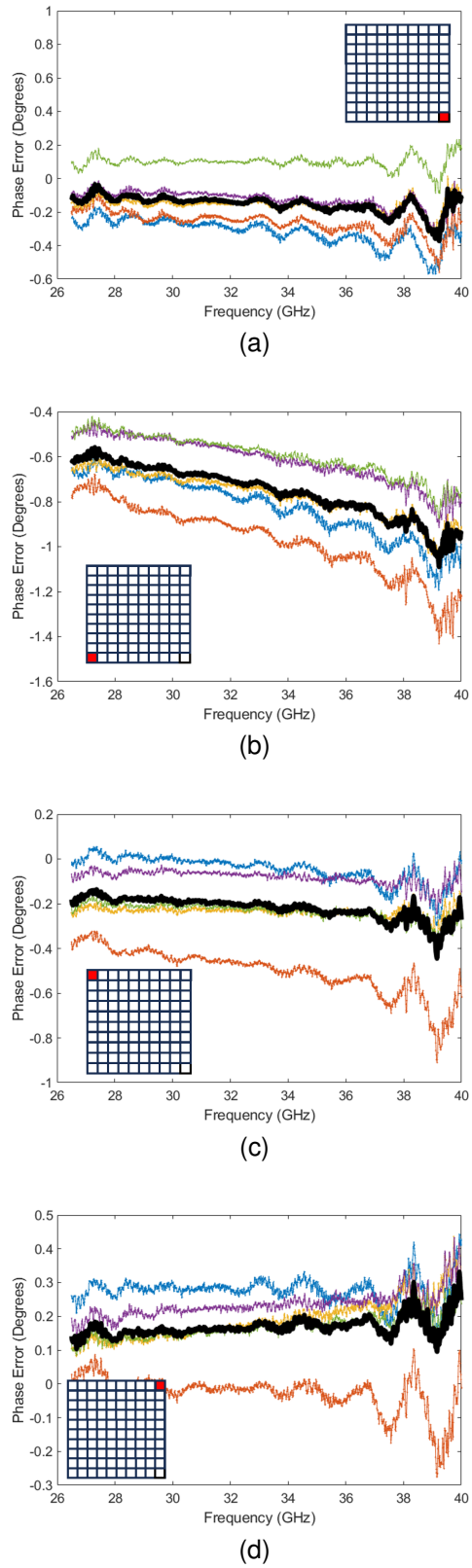

Fig. 10. Position-related differences in the phase $S_{64,P}$ (defined in Fig. 2a) due to fixture motion in a synthetic-aperture scan. Five calibrations with a 10 MHz VNA step size were performed over a 13-day period. These are shown by the thinner lines. The mean is shown by the thick black line. Four of the 121 array locations are shown, as indicated by the red square on the 11×11 grid inset.

used a natural-neighbor algorithm and was performed separately for horizontal and vertical polarizations.

Thus, we obtained a frequency dependent calibration matrix for each synthetic-aperture location and both polarizations. When combined with the other components of uncertainty, we obtain an associated distribution of uncertainty for our channel measurements. Note that the component of uncertainty due to fixture motion may be incorporated into any of the three calibration approaches described in the next section. Thus, precharacterization may be used.

IV. VNA CALIBRATION APPROACHES

Three common VNA calibration approaches utilizing three different calibration locations for OTA and channel measurements in an enclosed test chamber were introduced in Fig. 1. For each of these approaches, it is possible to precharacterize many components of uncertainty by the use of the two-tier calibration technique discussed in Sections II and III, saving time during the subsequent chamber characterization or channel measurement. Each of the three approaches discussed below may be used both for static measurements in which the antennas are stationary or when the measurement includes stepped antenna motion, as is encountered with the use of a turntable or robotic arm for synthetic-aperture measurement.

We next describe the three calibration approaches illustrated in Fig. 1 and some of the trade-offs associated with each in terms of convenience, efficiency and uncertainty. The components of uncertainty associated with each approach are provided in tabular form. Methods for determining these various components of uncertainty were detailed in Section III.

A. Approach A: Calibration at the Antenna Fixture

In some chamber set-ups, access to the antenna fixtures within the chamber is straightforward and the user can easily connect VNA calibration standards directly there, without disconnecting the cable attached to the antenna. Due to the stability of this set-up, repeatability uncertainty due to reconnection can be extremely small (as illustrated in Fig. 4), and so this approach may provide a low uncertainty, as discussed next.

The first-tier calibration consists of connecting waveguide standards to the coax-to-waveguide adapters that are mounted on fixtures shown by the black dotted reference planes in Fig. 1. The thru-standard measurement may be performed by disconnecting the cable from one fixture and connecting it to the cable at the other fixture. When TX and RX antenna fixtures are physically near to each other, the uncertainty due to this cable movement is minimal. For longer cable runs, the Thru measurement may be performed at the door prior to attaching the cables to the fixtures and treated as a reciprocal Thru [27]. This eliminates the impact of cable bending in the calibration, as the model used in the calibration only assumes equal forward and reverse transmission through the Thru standard.

This approach can provide the lowest uncertainty of the three approaches presented here. However, it requires access to the antenna fixtures, which may be difficult inside of a test chamber. As well, the calibration standards are measured at the end of the TX and RX cables and, thus, this approach is potentially impacted by low SNR. Components of uncertainty related to the VNA calibration are listed in Table I.

TABLE I
COMPONENTS OF UNCERTAINTY FOR APPROACH A

Components of Uncertainty	Section in paper	Comments
Drift	III-A	Before and after first-tier waveguide calibrations at the coax-to-waveguide adapters mounted to the antenna fixture
Mechanical Standards	III-A	Dimensional uncertainties of waveguide calibration standards
Calibration Repeatability and Noise	III-B	Second-tier calibrations obtained by repeating the waveguide calibrations at the adapters mounted to the antenna fixture
Fixture motion (if applicable))	III-E	Second-tier waveguide calibrations at the coax-to-waveguide adapters mounted to the antenna fixture on the robotic arm

B. Approach B: Calibration at the Chamber Door

In many cases, it is more convenient to detach the cables from the antenna fixtures and perform the VNA calibration at the door of the test chamber. Cable movement during this process may increase the uncertainty in subsequent measurements. For this method, the first-tier VNA calibration used during the channel or DUT measurement consists of connecting calibration standards to the ends of the coax-to-waveguide adapters at the door of the chamber shown by the blue dotted reference planes with x-symbols in Fig. 1.

This method has the advantage of convenience for the user because the coax-to-waveguide adapters are brought to the door of the chamber rather than having to calibrate at the antenna fixture within the chamber. However, it generally results in a higher uncertainty due to cable movement during and after calibration. The components of uncertainty related to the Approach B VNA calibration are listed in Table II. Note that calibration repeatability is not included in Table II because it is effectively included when the standards are connected to the cables.

TABLE II
COMPONENTS OF UNCERTAINTY FOR APPROACH B

Components of Uncertainty	Section in paper	Comments
Drift	III-A	Before and after first-tier waveguide calibrations at the end of the TX or RX cable, placed at the door of the chamber
Mechanical Standards	III-A	Dimensional uncertainties of WR28 calibration standards
Calibration Reproducibility	III-C	Second-tier calibrations obtained by attaching calibration standards at the door and at the fixture
Fixture motion (if applicable))	III-E	Second-tier waveguide calibrations at the coax-to-waveguide adapters mounted to the antenna fixture on the robotic arm

C. Approach C: Calibration at the VNA with Cable De-embedding

For measurements for which calibration inside the chamber is difficult and precharacterized cables are used, another option is to calibrate at the VNA ports and separately de-embed the precharacterized cables between the VNA and the antenna fixtures. Of course, this requires that the same cable and similar setup were used during the precharacterization and measurement phases of the process.

For this method, the cable's characteristics are precharacterized and are cascaded with subsequent first-tier calibrations performed at the external ports of the VNA. The first-tier VNA calibration conducted before and after the channel or DUT measurement consists of connecting coaxial standards to the VNA ports and performing the calibration as shown by the red dotted reference planes with circles in Fig. 1. The cables and coax-to-waveguide adapters are subsequently de-embedded in post processing as discussed in Section III-D.

A clear advantage of this approach is that, after precharacterizing the cables and adapters, the user only needs to calibrate at the VNA ports. Calibration at the VNA ports is often easy to perform and provides good SNR. However, cable and adapter precharacterization is time-consuming. The components of uncertainty related to the Approach C VNA calibration are listed in Tables III, IV, and V.

TABLE III
COMPONENTS OF UNCERTAINTY FOR APPROACH C, CABLE MEASUREMENTS

Components of Uncertainty Step 1: Cable Measurement	Section in paper	Comments
Drift	III-A	Before and after first-tier coaxial calibrations at the VNA ports
Mechanical Standards	III-A	Dimensional uncertainties of coaxial calibration standards
Calibration Reproducibility	III-C	Second-tier calibrations obtained by attaching calibration standards at the VNA ports, moving the cable to the antenna fixture and then recalibrating back at the VNA port

TABLE IV
COMPONENTS OF UNCERTAINTY FOR APPROACH C, COAX-TO-WAVEGUIDE ADAPTER MEASUREMENTS

Components of Uncertainty Step 2: Coax-to-Waveguide Adapter Measurement	Section in paper	Comments
Drift	III-A	Before and after first-tier coaxial calibrations at the VNA ports
Mechanical Standards	III-A	Dimensional uncertainties of both coaxial waveguide calibration standards
Calibration Repeatability and Noise: Coaxial Standards	III-B	Second-tier calibrations obtained by repeating the coaxial calibrations at the VNA ports
Calibration Repeatability and Noise: Waveguide Standards	III-B	Second-tier calibrations obtained by repeating the coaxial calibrations at the VNA ports

TABLE V
COMPONENTS OF UNCERTAINTY FOR APPROACH C, VNA CALIBRATION FOR CHANNEL OR DUT MEASUREMENT

Components of Uncertainty Step 3: VNA Calibration for Channel or DUT Measurement	Section in paper	Comments
Drift	III-A	Before and after first-tier coaxial calibrations at the VNA ports
Mechanical Standards	III-A	Dimensional uncertainties of coaxial calibration standards
Calibration Repeatability and Noise	III-B	Second-tier calibrations obtained by repeating the coaxial calibrations at the VNA ports
Cable de-embedding	III-D	From Step 1
Adapter de-embedding	III-D	From Step 2
Fixture motion (if applicable))	III-E	Second-tier waveguide calibrations at the coax-to-waveguide adapters mounted to the antenna fixture on the robotic arm

D. Incorporating Precharacterized Uncertainties from Second-Tier Calibration Matrices

As discussed, the uncertainties derived from the second-tier calibrations may be propagated into measurements performed at a later date by cascading the appropriate calibration matrices with the measured S-parameters. The use of a calibration routine such as the NIST Microwave Uncertainty Framework provides a mechanism for cascading any number of calibration matrices along with the systematic component of uncertainty due to non-ideal calibration standards.

To illustrate the order-of-magnitude differences in uncertainty that may be expected from Approaches A, B, and C, we performed VNA calibrations on a 1 MHz frequency grid between 26 and 40 GHz. The cable and adapter configuration outside the chamber is shown in Fig. 7. The VNA ports were 2.4 mm, with port 2 immediately adapted to 2.92 mm in order to precharacterize the 2.92-mm-to-WR-28 adapters that we used at the antenna fixtures. Inside the chamber, 2.92 mm coaxial cables connected to the coax-to-waveguide adapters.

The transmit antenna was a WR-28 open-ended waveguide mounted on a fixture at one end of the chamber. The receive antenna, also an open-ended waveguide, was mounted on the robotic arm shown in the photographs of Fig. 9. The wide beamwidth of the open-ended waveguide minimized the effects of the antenna pattern on the strength of the spatially distributed received signal.

Fig. 11 shows the combined standard uncertainty in phase for VNA calibration Approaches A–C described above for a measurement of the chamber's transfer function without antenna-fixture motion. We focus on the phase error because knowledge of the uncertainty in phase is critical for synthetic-aperture measurements, as will be illustrated in the next section.

As expected, the uncertainty from Approach A is the lowest,

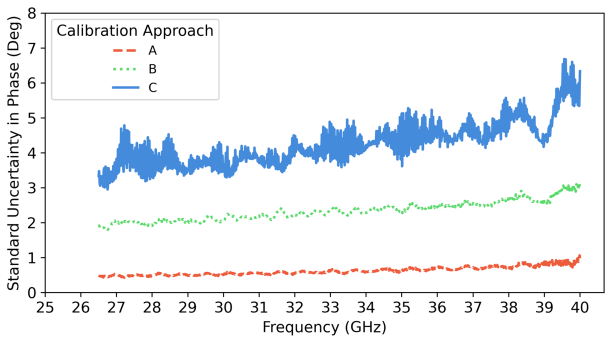

Fig. 11. An example of the combined phase uncertainty for VNA calibration approaches A–C described in Section IV.

with less than 1° in phase error across the measured band. The uncertainty in Approach B, with less than approximately 2° in phase error across the measured band, is lower than Approach C, with phase uncertainties up to approximately 6° at 40 GHz. Naturally, the results here are for a single OTA chamber set-up and can vary greatly for different set-ups and frequency ranges. Propagating these uncertainties into metrics of interest for OTA or channel test, including applications with fixture motion, will be illustrated in Section V.

V. MILLIMETER-WAVE MEASUREMENT EXAMPLE OF CALIBRATION USE CASES

We illustrate the application of the three VNA calibration approaches to the measurement of a reflective channel created in a hybrid anechoic/reverberant environment. This chamber provides a well-characterized, repeatable multipath test environment for wireless device performance assessment. We compute the uncertainty in both a single-antenna measurement and a synthetic-aperture measurement performed in the same reflective channel. The uncertainty due to fixture motion is incorporated into the synthetic-aperture case because it is based on scanning of the receive antenna over a two-dimensional array.

A. Chamber-Measurement Set-up and Analysis Procedure

The hybrid anechoic/reverberant chamber was configured to emulate the spatial characteristics observed in an industrial facility that was representative of a factory "work cell" having dimensions on the order of 3 m^3 [28]. Such work-cell channel conditions include strong specular reflections arriving from a wide range of angles of arrival over a relatively short time window. In our hybrid chamber, reflective spheres mounted on linear translation stages create the specular reflections at angles of arrival extracted from measurements that we performed in an industrial environment. The placement of the spheres to was optimized to match the desired angles by use of a machine-learning algorithm [29].

The VNA set-up was described in Section III and the three reference planes for the chamber measurements were shown in Fig. 1. A two-dimensional 12.75 cm by 12.75 cm synthetic-aperture array comprised of 35×35 elements was implemented using the robotic arm shown in the photographs of Fig. 9. Vertical and horizontal spacing of the array elements was 3.75 mm, equal to approximately $\lambda/2$ at 40 GHz. Measurements were performed with a frequency step of 10 MHz over the frequency range of 26.5–40 GHz with an IF bandwidth of 100 Hz These 1351 frequency points measured with the VNA over the 1225 array points required approximately 10 hours. For each VNA calibration approach, we measured the calibration standards at the indicated reference planes for the first-tier VNA calibration. Next, we performed the channel measurements, scanning the robotic arm over the two-dimensional 35×35 grid. Finally, we carried out a second set of first-tier calibrations to assess drift of the measurement setup.

In post processing, the appropriate components of uncertainty, given in Tables I–V of Section IV, were combined. As discussed in Section IV, we used the NIST Microwave Uncertainty Framework, which allows the propagation of uncertainty through multiple domains while maintaining the correlations between components of uncertainty.

To illustrate the uncertainty for different calibration approaches, in Section V-B we apply calibration approaches A–C to S-parameters measured at a single receive-antenna location at the center of the 35×35 array. These uncertainties do not include fixture motion. The differences in uncertainty in the measured power-delay profile are readily apparent. Then in SectionV-C, we include fixture motion with a synthetic-aperture analysis [19] of the 35×35 array of S-parameter data. These data are also calibrated using approaches A–C and the uncertainty in the angles of arrival of the primary reflections are calculated. For this case, we show that the uncertainty due to fixture motion has a negligible effect on the estimated angles of arrival.

B. Uncertainty for Different Calibration Approaches: Single-Antenna Measurement of Power Delay Profile

To illustrate the uncertainty in a single-antenna channel measurement, we propagate the components of VNA-calibration uncertainty through to the power-delay profile (PDP) of the measured reflective channel within the hybrid test chamber. Power delay profiles illustrate the relative time delays at which the reflected signal components arrive the receive antenna. PDPs computed from channel measurements in field tests of reflective environments are commonly used to create channel models that are representative of various multipath channel conditions [30]–[32]. PDPs are also used to characterize specific channel conditions replicated in the laboratory in order to expose devices to specific impairments [12], [16], [17], [29], as we have done here.

The PDP, represented as a normalized power as a function of delay τ is related to the magnitude-squared of the complex impulse response of the channel with

$$P(\tau) = |h(\tau)|^2, \tag{1}$$

where the normalized linear magnitude $|h(\tau)|$ is computed from the inverse Fourier transform of the measured, calibrated S-parameters S_{12} and S_{21} of the channel.

Fig. 12a shows the PDP of the reflective channel computed from 1, derived from S-parameters of the channel calibrated

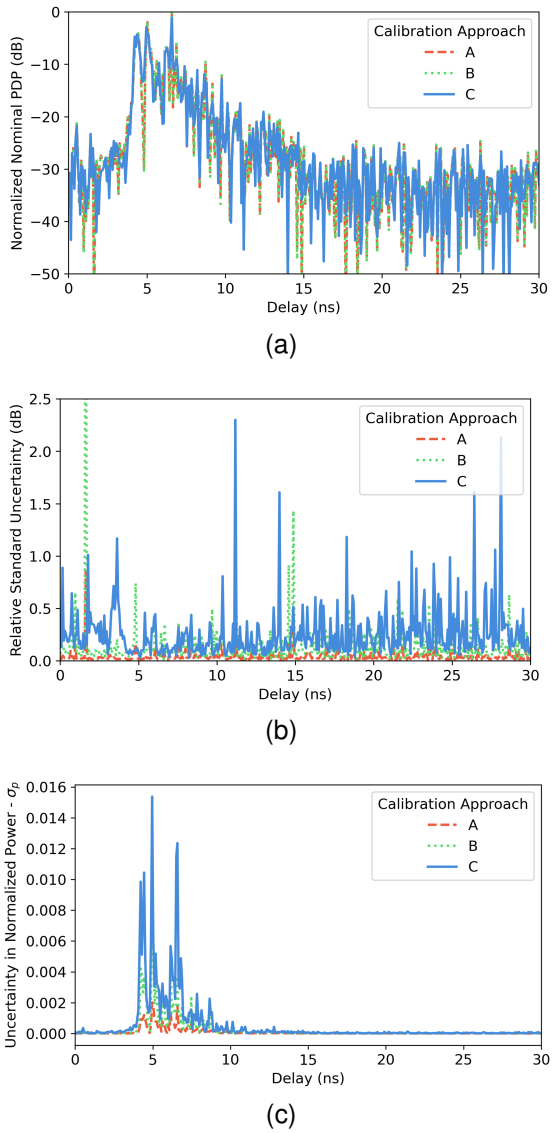

Fig. 12. Over-the-air measurements of a reflective channel performed in a hybrid anechoic/reverberation test chamber. (a) The power delay profile calibrated with Approaches A–C. (b) The relative standard uncertainty and (c) the normalized uncertainty in power on a linear scale.

with Approaches A–C and plotted in decibels. In Fig. 12a, the maximum value of the PDP, which occurs at a delay of approximately 6.5 ns, is approximately normalized to 1. We used Monte-Carlo simulations implemented in the NIST Microwave Uncertainty Framework to evaluate the uncertainties of the PDP in Figs. 12b and 12c. Figure 12b shows the uncertainty of the PDP relative to the value of the PDP at the same delay plotted in decibels. Fig. 12c shows the uncertainty in the linear power of the PDP at each delay, where the total power in the PDP has been normalized to 1. These uncertainties were calculated by propagating each complex Monte Carlo result through the power calculations to obtain a scalar result (e.g., decibel representation of a normalized power) and then computing the sample standard deviation of the Monte Carlo distribution of these scalar results. This functionality is standard in the NIST Microwave Uncertainty Framework.

As expected, calibration Approach A (Section IV-A) has the lowest uncertainty because the calibration standards were connected at the antenna fixture, eliminating uncertainty due to cable bending. Approach B (Section IV-B), where the coax-to-waveguide adapters were disconnected from the fixture and calibration standards connected at the door of the chamber, exhibits the next-highest overall uncertainty. Finally, Approach C (Section IV-C), with calibration performed at the VNA ports and cables/adapters subsequently de-embedded, has the highest overall uncertainty. This is because the uncertainties associated with the cable and adapter measurements are included in the analysis, as discussed in Section III-D.

The representations of uncertainty in Figs. 12b and 12c each have their strengths and weaknesses. The relative uncertainty in Fig. 12b represents the offset or "error bars" that would surround the PDP on the decibel scale. This representation shows a noticeable increase in uncertainty for weak received signals, for example at delays of approximately 4.9 ns and 15 ns for Approaches A and B, and 11 ns for Approach C. This increase in uncertainty occurs when the received signal approaches the noise floor of the receiver.

The uncertainty in the normalized power in Fig. 12c allows the user to clearly see the small value of uncertainty corresponding to weak values of received signal. This representation allows a user to clearly visualize the impact of the measurement setup on the quantity of interest, in this case the received signal in the delay domain. However, the result is plotted on a linear scale, which can complicate analysis.

TABLE VI
ANGLES OF ARRIVAL IN AZIMUTH (AZ) AND ELEVATION (EL) FOR ONE OF FOUR PRIMARY REFLECTIONS IN SYNTHETIC-APERTURE MEASUREMENT OF FIG. 13. "DIFF" CORRESPONDS TO CORRECTED – UNCORRECTED NOMINAL.

	AZ 1 (deg)	EL 1 (deg)
Cal A Diff	0.0047	0.0048
Cal A Std Dev	0.0004	0.0004
Cal B Diff	0.0047	0.0048
Cal B Std Dev	0.0006	0.0009
Cal C Diff	0.0075	0.0098
Cal C Std Dev	0.0008	0.0022

C. Uncertainty for Different Calibration Approaches: Synthetic-Aperture Measurement of Angle of Arrival

We next illustrate the effect of VNA calibration uncertainty on the calculated angle of arrival of the primary reflections by use of the synthetic-aperture measurement system with a movable antenna fixture. We propagated the combined uncertainties associated with calibration Approaches A, B, and C through to the measured angle of arrival of the four main reflections. For this analysis, we also included the uncertainty due to fixture motion described in Section III-E.

Fig. 13 shows a two-dimensional "heatmap" representation of the measured reflective channel. Recall that the TX and RX antennas for this measurement were WR-28 open-ended waveguides as discussed in Section IV-D. The robotic arm held the antenna fixture that, in turn, held the RX antenna. An RF

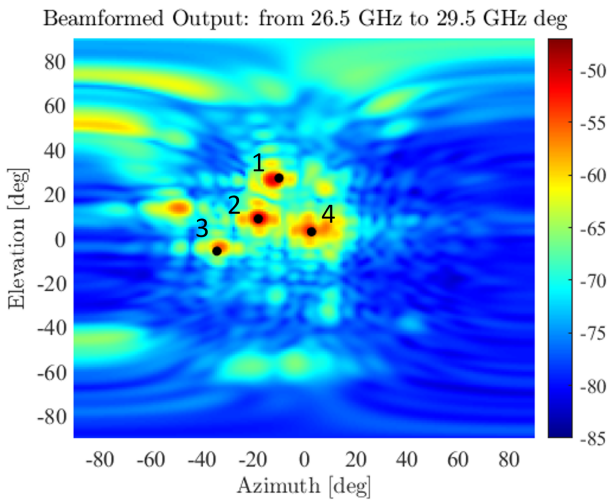

Fig. 13. Measured channel in a hybrid reflective/anechoic chamber showing reflections from four intentional reflectors, and non-ideal reflections from the chamber setup. Because the VNA is calibrated to the input ports of the antennas, the dB color scale includes the frequency-averaged pattern gain of the 35×35 element synthetic-aperture array, angle-dependent TX and RX antenna gains and path loss of the channel at each elevation and azimuth angle.

absorber was mounted to block reflections from the robotic arm such that only the RX antenna protruded out to face the reflective spheres [16]. The uncertainty associated with any reflections from this setup was inherently included in our uncertainty analysis. We attempted to separate this component of uncertainty, but these measurements will be part of our future work.

For the reflective channel measurement, synthetic-aperture beamforming was carried out on a grid with one-degree spacing in azimuth and elevation. The azimuth and elevation angles of arrival of the four desired reflections are indicated by black dots. Measured signal power is indicated by various colors. The angles of arrival of stronger received signals are indicated by darker red, and weaker signals by blue, as shown on the color scale on the right side of Fig. 13. We then computed the angles of arrival with a simple peak search over all azimuth and elevation pairs on the heat map.

To estimate the angles of arrival for the four strongest reflections and their corresponding uncertainties, 100 Monte Carlo samples were generated for each calibration approach using the NIST Microwave Uncertainty Framework, incorporating distributions of the uncertainties described in Section IV. Each of the 100 sets of Monte Carlo samples were then fed into the angle-of-arrival (AoA) analysis code, resulting in a distribution of azimuth and elevation angles. Results for Sphere 1 are presented in Table VI and the distribution of azimuthal angles is shown graphically in Fig. 14. Results for the other spheres were similar.

Recall that the precharacterized uncertainty due to fixture motion described in Section III-E included a systematic phase offset due to cable bending during fixture motion. The Microwave Uncertainty Framework allows for correction of such systematic errors. Thus, in Table VI, the uncorrected "nominal" value represents the estimate of AoA uncorrected for fixture-motion errors; the mean value of Monte Carlo distribution represents our best estimate of the angle of arrival after correction for fixture motion errors; and the standard deviation of this AoA distribution corresponds to the uncertainty in the estimate corrected for fixture-motion errors. It is clear that the differences between uncorrected and mean corrected values are extremely small, as are the standard deviations of the distributions. This is largely due to the modest cable bending that occurs during fixture motion, and the relatively large array size (180.31 mm on the diagonal), corresponding to roughly 17λ at 28 GHz and 24λ at 40GHz (where $\lambda \approx$ 10.7 mm at 28 GHz and $\lambda \approx$ 7.5 mm at 40 GHz). However, the uncorrected values are well outside of the Monte-Carlo distribution shown in Fig. 14, indicating that it is nevertheless important to apply the correction in the analysis.

Components of uncertainty that are applied equally to all locations in the synthetic-aperture array do not affect the AoA because synthetic-aperture algorithms compute the relative differences in phase measured at each aperture location. Thus, the only components of uncertainty that impact the AoA correspond to the fixture motion. Table VI shows this to be a small effect.

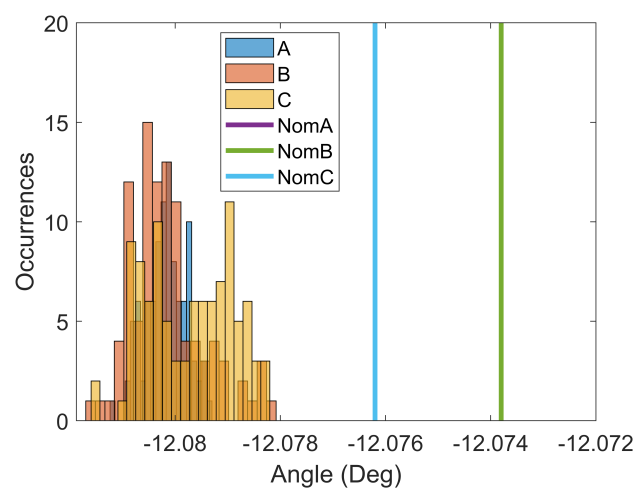

Fig. 14. Histogram of the estimated azimuth angle of arrival of reflections from Sphere 1 shown in Fig. 13 compared to the uncorrected nominal values for the three calibrations. Note that the nominal values from approaches A and B, referred to as NomA and NomB at the far right of the graph are identical.

Fig. 14 illustrates this graphically by plotting the distribution in azimuth for the angles of arrival of reflections from Sphere 1. The mean values for calibration approaches A and B are identical. While we would expect all three approaches to provide identical AoAs, they are slightly different (on the order of 0.002 degree). This is likely due to frequency-dependent amplitude errors skewing the results of our beam-center search algorithm, which is amplitude based. The distribution of angles around the mean is also extremely small (on the order of 0.006 degree).

The small differences between the uncorrected nominal and corrected mean values of AoA indicate that the "best-practice" techniques developed for our synthetic-aperture measurements have paid off. These best practices include (as mentioned in Section III-D) allowing cables to relax and the chamber

to warm up for at least an hour between calibration and measurement and performing scans over a single polarization prior to changing polarization. However, it can be expected that other set-ups will have different levels of uncertainty. The techniques presented here are applicable in a wide range of OTA and channel test-chamber setups.

VI. Conclusion

The uncertainty in laboratory based OTA and channel measurements can impact the determination of crucial metrics such as received or radiated power, RMS delay spread, bit-error rate, error vector magnitude and angle of arrival. Uncertainties in the chamber characterization can also make it difficult to separate measurement setup equipment imperfections from DUT imperfections.

We presented an approach for assessing components of uncertainty introduced during the VNA calibration process that are commonly encountered in OTA and channel test-chamber measurements. We illustrated the utility of a second-tier calibration approach for pre-characterizing difficult or time-consuming components of uncertainty related to VNA repeatability, reproducibility, fixture motion, and cable de-embedding. We illustrated how these uncertainties would be applied to the chosen calibration reference plane. We then extracted key parameters (e.g. the variance of the amplitudes and phases of the transmission parameters of the various calibration matrices) to evaluate the relative impact of VNA calibration uncertainties such as cable bending and connector repeatability on measured results of a multipath channel.

Throughout the work, we discussed the trade-offs between convenience of calibration with measurement uncertainty in the use of different calibration reference planes. Such comparisons allow the user to make informed decisions on the optimal location of the calibration reference plane, given the unique constraints of VNA measurements performed in OTA and channel test chambers.

Appendix

We have extensively used the software referred to as the NIST Microwave Uncertainty Framework [25] for our uncertainty analysis. To quote [25], it "provides a drag-and-drop toolkit for managing the calculation of uncertainties in VNA and other measurements." It is particularly useful because it allows for the propagation of uncertainties while capturing any correlations.

In this work, we use it to propagate uncertainty through cascades of the various calibration matrices to our chamber-characterization or channel measurements. The calculations shown here can be independently represented by 2×2 matrices since there are no coupling terms in the calibration matrices. We have chosen our approach because using 4×4 matrices simplifies the analysis in the NIST Microwave Uncertainty Framework that can also handle the coupling terms. To better understand how this is accomplished in the NIST Microwave Uncertainty Framework, when there are no coupling terms in the calibration matrices, we can break the 4×4 scattering-parameters of each of the calibration matrices into two 2×2 scattering-parameter matrices, as illustrated in Fig. 15. We can then use standard T-parameter representations to perform the cascading operation on the two halves of the 4×4 calibration matrices and reassemble the resultant 4×4 calibration matrix from the two 2×2 results.

For example, to cascade the 4×4 scattering-parameter calibration matrices $[S]_{\mathrm{Ref}}$ and $[S]_{\mathrm{P}}$ shown in Fig. 15, we can start with port 1 and define $[S]_{\mathrm{Ref1}}$ and $[S]_{\mathrm{P1}}$ as

$$[S]_{\mathrm{Ref1}} = \begin{bmatrix} S_{11,\mathrm{Ref}} & S_{13,\mathrm{Ref}} \\ S_{31,\mathrm{Ref}} & S_{33,\mathrm{Ref}} \end{bmatrix}, \tag{2}$$

$$[S]_{\mathrm{P1}} = \begin{bmatrix} S_{33,\mathrm{P}} & S_{35,\mathrm{P}} \\ S_{53,\mathrm{P}} & S_{55,\mathrm{P}} \end{bmatrix}, \tag{3}$$

where the subscripts "Ref1" and "P1" denote the port 1 measurements. We can then calculate the T-parameter representations of $[S]_{\mathrm{Ref1}}$ and $[S]_{\mathrm{P1}}$ as

$$[S]_{\mathrm{Ref1}} \xrightarrow{\text{S to T}} [T]_{\mathrm{Ref1}}, \tag{4}$$

$$[S]_{\mathrm{P1}} \xrightarrow{\text{S to T}} [T]_{\mathrm{P1}}. \tag{5}$$

The T-parameter representation allows us to calculate the cascade $[S]_{\mathrm{RefP1}}$ of $[S]_{\mathrm{Ref1}}$ and $[S]_{\mathrm{P1}}$ as

$$[T]_{\mathrm{RefP1}} = [T]_{\mathrm{Ref1}}[T]_{\mathrm{P1}}, \tag{6}$$

$$[T]_{\mathrm{RefP1}} \xrightarrow{\text{T to S}} [S]_{\mathrm{RefP1}}. \tag{7}$$

Now we can use $[S]_{\mathrm{RefP1}}$ to fill the first half of $[S]_{\mathrm{RefP}}$ with the substitutions $[S]_{11,\mathrm{RefP}} = [S]_{11,\mathrm{RefP1}}$, $[S]_{31,\mathrm{RefP}} = [S]_{21,\mathrm{RefP1}}$, $[S]_{13,\mathrm{RefP}} = [S]_{12,\mathrm{RefP1}}$ and $[S]_{33,\mathrm{RefP}} = [S]_{22,\mathrm{RefP1}}$.

A similar procedure is used to fill the second half of $[S]_{\mathrm{RefP}}$ with the substitutions $[S]_{44,\mathrm{RefP}} = [S]_{11,\mathrm{RefP2}}$, $[S]_{64,\mathrm{RefP}} = [S]_{21,\mathrm{RefP2}}$, $[S]_{46,\mathrm{RefP}} = [S]_{12,\mathrm{RefP2}}$ and $[S]_{66,\mathrm{RefP}} = [S]_{22,\mathrm{RefP2}}$. The NIST Microwave Uncertainty Framework uses similar computations internally that include the coupling terms to cascade and de-embed calibration matrices.

Acknowledgments

The authors thank Angela Stelson, Lucas N. Koepke, Michael Frey, Richard Candell, and Iyemeh Uchendu for helpful technical comments and suggestions.

References

[1] CTIA Certification, "CTIA 01.20 test methodology, SISO, anechoic chamber," *Test Plan for Wireless Device Over-the-Air Performance, v.6.0.3*, p. 65, Dec. 2024, accessed: August 1, 2025.

[2] CTIA Certification and WiFi Alliance, "Test plan for RF performance evaluation of Wi-Fi mobile converged devices," *Test Plan for Wireless Device Over-the-Air Performance, v.6.0.1*, p. 91, Nov. 2024, accessed: August 1, 2025.

[3] CTIA Certification, "CTIA 01.22 test methodology, SISO, millimeter wave," *Test Plan for Wireless Device Over-the-Air Performance, v.6.0.0*, p. 65, Mar. 2023, accessed: August 1, 2025.

[4] S. L. Smith, J. W. Archer, G. P. Timms, K. W. Smart, S. J. Barker, S. G. Hay, and C. Granet, "A Millimeter-Wave Antenna Amplitude and Phase Measurement System," *IEEE Transactions on Antennas and Propagation*, vol. 60, no. 4, pp. 1744–1757, Apr. 2012, doi: 10.1109/TAP.2012.2186218.

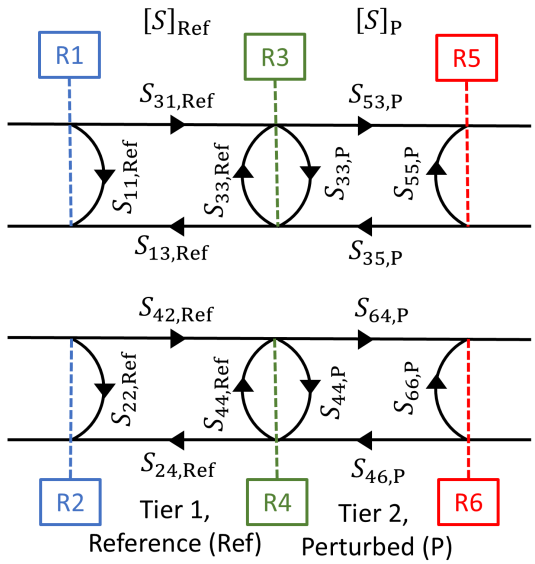

Fig. 15. Flow-graph illustrating the cascade of first-tier (Tier 1) and second-tier (Tier 2) calibration matrices.

[5] Y. Li, F. Zhang, K. Olesen, Z. Ying, G. F. Pedersen, and W. Fan, "An Automated Over-the-Air Radiated Testing Platform for Reconfigurable Intelligent Surface," in *2024 18th European Conference on Antennas and Propagation (EuCAP)*, Mar. 2024, pp. 1–5, doi: 10.23919/EuCAP60739.2024.10501131.

[6] CTIA Certification, "CTIA 01.21 test methodology, SISO, reverberation chamber, informational," *Test Plan for Wireless Device Over-the-Air Performance, v.6.0.1*, p. 22, Sep. 2023, accessed: August 1, 2025.

[7] K. A. Remley, J. Dortmans, C. Weldon, R. D. Horansky, T. B. Meurs, C.-M. Wang, D. F. Williams, C. L. Holloway, and P. F. Wilson, "Configuring and Verifying Reverberation Chambers for Testing Cellular Wireless Devices," *IEEE Transactions on Electromagnetic Compatibility*, vol. 58, no. 3, pp. 661–672, Jun. 2016, doi: 10.1109/TEMC.2016.2549031.

[8] P.-S. Kildal, X. Chen, C. Orlenius, M. Franzen, and C. S. L. Patane, "Characterization of Reverberation Chambers for OTA Measurements of Wireless Devices: Physical Formulations of Channel Matrix and New Uncertainty Formula," *IEEE Transactions on Antennas and Propagation*, vol. 60, no. 8, pp. 3875–3891, Aug. 2012, doi: 10.1109/TAP.2012.2201125.

[9] D. Senic, K. A. Remley, C.-M. J. Wang, D. F. Williams, C. L. Holloway, D. C. Ribeiro, and A. T. Kirk, "Estimating and Reducing Uncertainty in Reverberation-Chamber Characterization at Millimeter-Wave Frequencies," *IEEE Transactions on Antennas and Propagation*, vol. 64, no. 7, pp. 3130–3140, Jul. 2016, doi: 10.1109/TAP.2016.2556711.

[10] A. A. Ruiz, S. Hosseinzadegan, J. Kvarnstrand, K. Arvidsson, and A. A. Glazunov, "A Practical Approach to Generating First-Order Rician Channel Statistics in an RC Plus CATR Chamber at mmWave Frequencies," *IEEE Transactions on Antennas and Propagation*, vol. 73, no. 4, pp. 2120–2134, Apr. 2025, doi: 10.1109/TAP.2024.3502904.

[11] M. G. Becker, R. D. Horansky, D. Senic, V. Neylon, and K. A. Remley, "Spatial channels for wireless over-the-air measurements in reverberation chambers," in *12th European Conference on Antennas and Propagation (EuCAP 2018)*, Apr. 2018, pp. 1–5, doi: 10.1049/cp.2018.0854.

[12] M. Kashef, K. A. Remley, P. Manurkar, J. M. Kast, I. E. Uchendu, R. D. Horansky, M. Simons, M. Frey, L. Koepke, and R. Candell, "Standardizable approach for assessing wireless IoT devices in millimeter-wave industrial work-cell channels," *in progress*.

[13] M. Dawood Al-Dabbagh, T. Doeker, T. Kleine-Ostmann, T. Kürner, and D. Humphreys, "THz Channel Sounder and VNA Verification Measurement Based Over-the-Air Multipath Artifact," in *2022 47th International Conference on Infrared, Millimeter and Terahertz Waves (IRMMW-THz)*, Aug. 2022, pp. 1–2, iSSN: 2162-2035, doi: 10.1109/IRMMW-THz50927.2022.9895510.

[14] B. T. Arnold and M. A. Jensen, "Reconfigurable Over-the-Air Chamber for Mobile Device Testing: Analysis and Design," *IEEE Transactions on Antennas and Propagation*, vol. 71, no. 11, pp. 8964–8974, Nov. 2023, doi: 10.1109/TAP.2023.3312937.

[15] O. A. Iupikov, P. S. Krasov, A. A. Glazunov, R. Maaskant, J. Fridén, and M. V. Ivashina, "Hybrid OTA Chamber for Multidirectional Testing of Wireless Devices: Plane Wave Spectrum Generator Design and Experimental Demonstration," *IEEE Transactions on Antennas and Propagation*, vol. 70, no. 11, pp. 10 974–10 987, Nov. 2022, doi: 10.1109/TAP.2022.3184516.

[16] J. M. Kast, P. Manurkar, S. Perera, M. K. Hany, R. D. Horansky, R. Candell, K. A. Remley, and M. T. Simons, "Laboratory-Based Reference Channels for Millimeter-Wave Wireless Device Measurements," in *2024 IEEE Conference on Computational Imaging Using Synthetic Apertures (CISA)*, May 2024, pp. 01–05, doi: 10.1109/TAP.2022.3184516.

[17] M. D. Al-Dabbagh, D. Ulm, T. Doeker, D. Dupleich, A. Ebert, R. S. Thomä, T. Kürner, D. A. Humphreys, and T. Kleine-Ostmann, "Characterization of Sub-THz Channel Sounding Systems in OTA Measurement Scenarios Using a Vector Network Analyzer," *IEEE Transactions on Antennas and Propagation*, vol. 73, no. 6, pp. 3943–3958, Jun. 2025, note: 10.1109/TAP.2025.3533887.

[18] A. A. Glazunov, "Over-the-Air Testing Environments with Spatial-Directional Selectivity for Characterizing Wireless Devices and Systems," in *2024 18th European Conference on Antennas and Propagation (EuCAP)*, Mar. 2024, pp. 1–5, doi: 10.23919/EuCAP60739.2024.10501110.

[19] P. Vouras, B. Jamroz, A. Weiss, D. F. Williams, R. Leonhardt, D. Guven, R. Jones, J. Kast, K. A. Remley, R. D. Horansky, and C. Gentile, "Wideband Synthetic-Aperture Millimeter-Wave Spatial-Channel Reference System With Traceable Uncertainty Framework," *IEEE Open Journal of Vehicular Technology*, vol. 4, pp. 325–341, 2023, doi: 10.1109/OJVT.2023.3239617.

[20] CTIA Certification, "CTIA 01.70 measurement uncertainty," *Test Plan for Wireless Device Over-the-Air Performance, v.6.0.3*, p. 83, 2023, accessed: August 1, 2025.

[21] R. Vaitkus and D. Scheitlin, "A Two-Tier Deembedding Technique for Packaged Transistors," in *1982 IEEE MTT-S International Microwave Symposium Digest*, Jun. 1982, pp. 328–330, iSSN: 0149-645X, doi: 10.1109/MWSYM.1982.1130708.

[22] G. Elmore, "De-Embedded Measurements Using the HP 8510 Microwave Network Analyzer," in *25th ARFTG Conference Digest*, vol. 7, Jun. 1985, pp. 124–143, doi: 10.1109/ARFTG.1985.323625.

[23] R. Marks and K. Phillips, "Wafer-Level ANA Calibrations at NIST," in *34th ARFTG Conference Digest*, vol. 16, Nov. 1989, pp. 11–25, doi: 10.1109/ARFTG.1989.323952.

[24] M. Frey, B. F. Jamroz, A. Koepke, J. D. Rezac, and D. Williams, "Monte Carlo sampling bias in the microwave uncertainty framework*," *Metrologia*, vol. 56, no. 5, p. 055003, Aug. 2019, publisher: IOP Publishing, doi: 10.1088/1681-7575/ab2c18.

[25] D. Williams and A. Lewandowski, "NIST Microwave Uncertainty Framework," *National Institute of Standards and Technology*, 2011. [Online]. Available: https://www.nist.gov/services-resources/software/wafer-calibration-software

[26] J. A. Jargon, C. Cho, D. F. Williams, and P. D. Hale, "Physical models for 2.4 mm and 3.5 mm coaxial VNA calibration kits developed within the NIST microwave uncertainty framework," in *2015 85th Microwave Measurement Conference (ARFTG)*, May 2015, pp. 1–7, doi: 10.1109/ARFTG.2015.7162913.

[27] A. Ferrero and U. Pisani, "Two-port network analyzer calibration using an unknown 'thru'," *IEEE Microwave and Guided Wave Letters*, vol. 2, no. 12, pp. 505–507, Dec. 1992, doi: 10.1109/75.173410.

[28] M. Kashef, P. Vouras, R. D. Jones, R. Candell, and K. A. Remley, "A Machine-Learning Approach for the Exemplar Extraction of mmWave Industrial Wireless Channels," *IEEE Open Journal of Instrumentation and Measurement*, vol. 1, pp. 1–15, 2022, doi: 10.1109/OJIM.2022.3181309.

[29] M. K. Hany, S. Perera, C. Nogueira, R. Candell, K. A. Remley, and M. T. Simons, "A Deep Reinforcement Learning Approach for Automated Chamber Configuration Replicating mmWave Directional Industrial Channel Behavior," in *2023 100th ARFTG Microwave Measurement Conference (ARFTG)*, Jan. 2023, pp. 1–6, doi: 10.1109/ARFTG56062.2023.10148878.

[30] 3rd Generation Partnership Project (3GPP), "Technical Specification Group Radio Access Network; Study on channel model for frequencies from 0.5 to 100 GHz (Release 18)," 2024, accessed: August 1, 2025. [Online]. Available: https://portal.3gpp.org/desktopmodules/Specifications/SpecificationDetails.aspx?specificationId=3173

[31] G. R. Maccartney, T. S. Rappaport, S. Sun, and S. Deng, "Indoor Office Wideband Millimeter-Wave Propagation Measurements and Channel Models at 28 and 73 GHz for Ultra-Dense 5G Wireless Net-

works," *IEEE Access*, vol. 3, pp. 2388–2424, 2015, doi: 10.1109/ACCESS.2015.2486778.

[32] S. Salous, J. Lee, M. D. Kim, M. Sasaki, W. Yamada, X. Raimundo, and A. A. Cheema, "Radio propagation measurements and modeling for standardization of the site general path loss model in international telecommunications union recommendations for 5G wireless networks," *Radio Science*, vol. 55, no. 1, pp. 1–12, Jan. 2020, doi: 10.1029/2019RS006924.

Paritosh Manurkar (Senior Member, IEEE) received the Ph.D. degree in electrical engineering from Northwestern University, Evanston, IL, USA, in 2016. He is currently a Senior Research Associate at the University of Colorado (CU) at Boulder, Boulder, CO, USA and performs his research at the National Institute of Standards and Technology (NIST), Boulder, through a CU-NIST Partnership. He is currently working with the Shared Spectrum Metrology Group in the RF noise measurement project. He has previously worked on development of precision, calibrated, millimeter-wave modulated-signal sources, performing traceable over-the-air measurements, channel sounding, time and frequency transfer between optical clocks, development of fully self-referenced fiber frequency combs, nonlinear optics experiments using shaped pulses, fabrication of infrared detectors, and semiconductor engineering. He is actively involved in standards development as the Chair of the IEEE P1765 Working Group, a member of the IEEE Synthetic Aperture Technical Working Group (SA-TWG), and a member of the IEEE Microwave Theory and Technology Society's (MTT-S) Standards Committee (SC).

Sudantha Perera (Member, IEEE) received the B.Sc. degree in Electrical Engineering from the University of Moratuwa, Sri Lanka, in 2005, the M.S. degree from California State University, Los Angeles, USA, in 2008 and the Ph.D. degree from the University of Oklahoma, USA, in 2016. He has worked as a Systems Engineer at Western Digital, as a Research Assistant and Postdoctoral Research Associate at the Advanced Radar Research Center (ARRC), University of Oklahoma, and as a Research Associate at the National Institute of Standards and Technology (NIST), Boulder, CO. Since 2024, he has been an Embedded Systems Engineer in Tracking Radar Systems at ARRC. His expertise includes tracking filters, Radar signal processing, MIMO radar development, array signal processing, and high-frequency measurement technologies.

Kate A. Remley (Life Fellow, IEEE) was born in Ann Arbor, MI. She received the Ph.D. degree in Electrical and Computer Engineering from Oregon State University, Corvallis, in 1999.

From 1983 to 1992, she was a Broadcast Engineer in Eugene, OR, serving as Chief Engineer of an AM/FM broadcast station from 1989-1991. In 1999, she joined the RF Technology Division of the National Institute of Standards and Technology (NIST), Boulder, CO, as an Electronics Engineer. She was the Leader of the Metrology for Wireless Systems Project at NIST from 2003 to 2022, where her research activities included development of calibrated measurements for microwave and millimeter-wave wireless systems and standardized over-the-air test methods for the wireless industry and public-safety sectors. In July 2022, she retired from NIST.

Dr. Remley was the recipient of the Department of Commerce Bronze and Silver Medals, an ARFTG Best Paper Award, the NIST Schlichter Award, and is a member of the Oregon State University Academy of Distinguished Engineers. She was the Chair of the MTT-11 Technical Committee on Microwave Measurements (2008-2010), the Editor-in-Chief of IEEE Microwave Magazine (2009-2011), and Chair of the MTT Fellow Evaluating Committee (2017-2018). She was a Distinguished Lecturer for the IEEE Electromagnetic Compatibility Society (2016-2017) and was the co-Technical Program Chair for the IEEE International Microwave Symposium IMS2022.

Dylan Williams (Life Fellow, IEEE) received a Ph.D. in Electrical Engineering from the University of California, Berkeley in 1986. He joined the Electromagnetic Fields Division of the National Institute of Standards and Technology in 1989 where he develops electrical waveform and microwave metrology. He has published over 140 technical papers. He is the recipient of the Department of Commerce Bronze and Silver Medals, the Astin Measurement Science Award, two Electrical Engineering Laboratory's Outstanding Paper Awards, three Automatic RF Techniques Group (ARFTG) Best Paper Awards, the ARFTG Automated Measurements Technology Award, the IEEE Morris E. Leeds Award, the European Microwave Prize and the 2013 IEEE Joseph F. Keithley Award. Dr. Williams also served as Editor of the IEEE Transactions on Microwave Theory and Techniques from 2006 to 2010, as the Executive Editor of the IEEE Transactions on Terahertz Science and Technology, and as the 2017 President of the IEEE Microwave Theory and Techniques Society.

Mohamed Kashef (Hany) (Member, IEEE) received the B.Sc. and M.S. degrees (with Hons.) in electronics and electrical communications engineering from the Cairo University, Cairo, Egypt, in June 2006 and August 2009, respectively, and the Ph.D. degree in electrical engineering from the University of Maryland at College Park, College Park, MD, USA, in 2013. He is currently a Research Scientist at the National Institute of Standards and Technology (NIST). His current focus is on industrial wireless systems including wireless networks deployment, channel modelling, applying artificial intelligence for data analysis and test methods for wireless networks in industrial scenarios. His research interests also include wireless communication systems and networks, visible light communication networks, and optimization of stochastic systems.

Joshua M. Kast (Member, IEEE) received the Ph.D. in electrical engineering from the Colorado School of Mines, Golden, CO, USA, in 2022. He joined the NIST Communications Technology Laboratory as a graduate student associate in 2017, and as an NRC postdoctoral associate in 2023. His research includes finite-difference methods for electromagnetic simulation, nonlinear vector network analyzer applications, X-Parameter device characterization, timing uncertainty, modulated signal characterization, synthetic-aperture applications, and electro-optic measurements. He is currently with the High-Speed Waveform Metrology group at NIST.

Robert D. Horansky (Member, IEEE) received the B.A. degree in chemistry and the Ph.D. degree in physics from the University of Colorado, Boulder, CO, USA, in 1999 and 2005, respectively. His thesis work focused on low-noise dielectric measurements on novel materials in molecular electronics. Since 2005, he has been with the National Institute of Standards and Technology (NIST), Boulder, CO, USA, where he started out developing the highest resolving power energy dispersive sensor to date. He then went on to develop metrology techniques for single photon sensors in nuclear radiation and optical power measurements. In 2015, he joined the Metrology for Wireless Systems Project in the Communications Technology Laboratory, NIST developing calibrations and traceability for millimeter-wave wireless systems and reverberation-chamber measurements for cellular applications. He is the Secretary of the IEEE P1765 Standards Working Group on Uncertainty for EVM, and the winner of two Department of Commerce Medals for research in LTE Factor Screening and Novel Single Photon Detectors.